IET Control Theory & Applications

Research Article

IET Journals
The Institution of Engineering and Technology

Design and implementation of an LCL grid-connected inverter based on capacitive current fractional proportional–integral feedback strategy

ISSN 1751-8644
Received on 24th January 2020
Revised 10th August 2020
Accepted on 25th August 2020
E-First on 21st October 2020
doi: 10.1049/iet-cta.2020.0103
www.ietdl.org

Qingyi Wang[1,2], Binlei Ju[1,2] ✉, Yiqiong Zhang[1,2], Dan Zhou[1,2], Nan Wang[3], Genping Wu[3]

[1]*School of Automation, China University of Geosciences, Wuhan, 430074, People's Republic of China*
[2]*Hubei Key Laboratory of Advanced Control and Intelligent Automation for Complex Systems, Wuhan, 430074, People's Republic of China*
[3]*Wuhan Second Ship Design and Research Institute, Wuhan, Hubei, 430064, People's Republic of China*
✉ *E-mail: jubinlei@163.com*

Abstract: The capacitive current feedback active damping strategy has a limited damping region. When the grid-side impedance is large, the digital control inductor–capacitor–inductor (LCL) grid-connected inverter system with grid-side current loop control and capacitive current feedback active damping cannot run stably. To address this issue, this study proposes an improved capacitive current feedback active damping strategy, namely the capacitive current fractional proportional–integral feedback strategy (CCFPIFS), which increases the upper-frequency limit of the system damping region and approaches to the Nyquist sampling frequency. Furthermore, this study analyses the constraints of fractional-order proportional–integral controller parameters to ensure the stability of the system. The simulation analysis is performed by Simulink. The experimental results are consistent with theoretical expectations. Consequently, the proposed CCFPIFS can not only achieve better control performance and improve the robustness of the LCL grid-connected inverter system, but also improve the output power quality of the system. This damping strategy can make the LCL grid-connected inverter system work stably under the environment of high grid impedance.

1 Introduction

With the depletion of conventional fossil energy sources and the aggravation of environmental pollution, new energy sources have received widespread attention. In the new energy grid-connected power generation system, grid-connected inverters play an extremely important role as the key power electronic devices connecting new energy power generation systems to the power grid. Since the grid-connected power generation system needs to meet the relevant standards in power quality [1–3] when connected to the grid, and usually cascade filters after the grid-connected inverter to improve the grid-connected power quality. Considering that inductor–capacitor–inductor (LCL) filters have better high-frequency performance and smaller filter size [4–6] than L and LC filters, LCL grid-connected inverters are widely used in the grid-connected power generation system. However, the inherent characteristics of LCL filters may cause system instability [7], which challenges the system damping strategy. Therefore, to ensure the stable operation of the system, a damped resonance scheme must be considered.

With the further development of LCL grid-connected inverter system stability analysis, many damping strategies are proposed, mainly including passive damping (PD) [8, 9] and active damping (AD) [10–12]. Active damping has become the focus of research due to its high transmission efficiency and improved output current waveforms. Among various AD strategies, based on the principle of the PD method, the capacitive current feedback strategy (CCFS) [11, 13], which achieves the damping effect by simulating the physical model of resistance, has become one of the most widely used methods due to its simplicity, high robustness, and good transient performance.

However, in the LCL grid-connected inverter system with current single-loop control, the digital control system is usually used in the implementation process, which will cause a digital delay of 1.5 beats [14]. At this time, the effect of CCFS is equivalent to a virtual frequency-dependent resistor and a virtual frequency-dependent reactor in parallel with the filter capacitor. The virtual resistor plays a role of damping the resonance peak, and the virtual reactor plays a role in shifting the resonance frequency. When the control amount of the current single loop is the grid-side current, the positive and negative intervals of the equivalent virtual resistor of CCFS in the frequency domain are $(f_s/6, f_s/2)$ and $(0, f_s/6)$ [15, 16]. When the resonance frequency f_r of the LCL filter is kept in the range of $(f_s/6, f_s/2)$, the equivalent virtual resistor is positive, and the system can guarantee stable operation [17]. In fact, due to the influence of grid impedance and virtual reactor, there is a certain offset between f_r and the actual resonance frequency f_r'. When $f_r' \in (0, f_s/6)$, the negative equivalent virtual resistor will bring two right half-plane unstable poles to the grid-connected inverter system, and the damping effect of CCFS is negative, resulting in system instability. Therefore, in the case of the weak grid and grid impedance changes, additional damping strategies are still needed to ensure the stable operation of the system.

To solve the various problems caused by the digital delay, the capacitive current feedback AD strategy can also play a good damping role in the case of grid impedance changes. There are three common methods at present, which are additional time delay compensation methods [18–20], additional digital filters methods [21, 22], and expanding the system damping region methods [23, 24]. The additional time delay compensation method reduces or predicts the digital delay, thereby reducing the negative effects of the digital delay, but the digital delay cannot be completely eliminated, and the control algorithms are mostly complicated or require many sensors. The method of adding digital filters uses the s-domain characteristics of the digital filter to change the system resonance peak. For example, Cai *et al*.[21] used the phase lag characteristics of the digital low-pass filter to make the system meet the amplitude and phase margin, thereby keeping the system stable. Pan *et al*. [22] used the 180° phase-frequency characteristic of the digital resonance-notch (biquad) filter to translate the resonance frequency into the damping region of the system. However, the digital filter design process needs to know the system

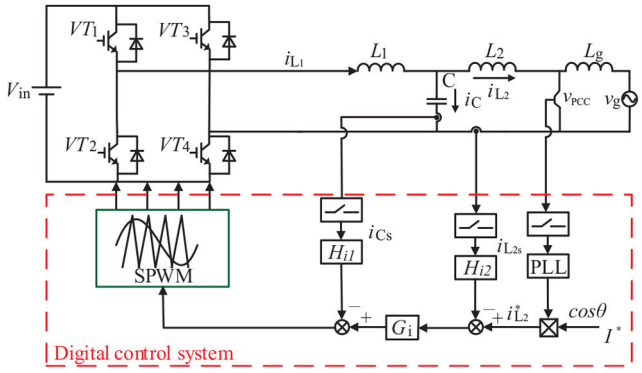

Fig. 1 *Main circuit and control block diagram of digitally controlled LCL single-phase grid-connected inverter system with CCFS*

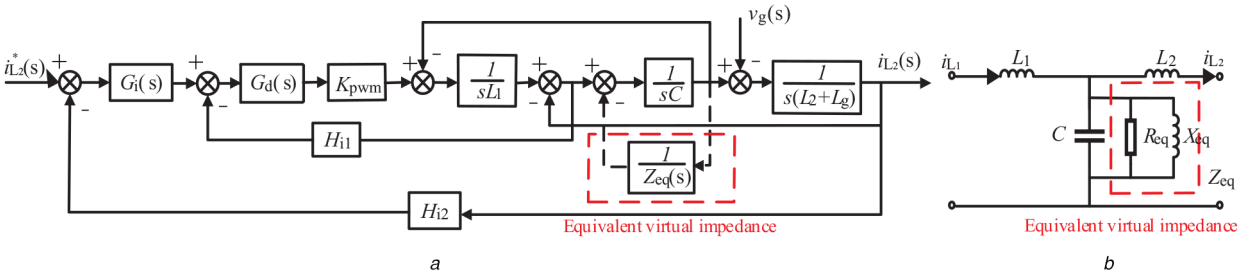

Fig. 2 *System model with CCFS*
(a) System control block diagram, ***(b)*** Equivalent circuit diagram

parameters, so the method of adding digital filters is more sensitive to the system parameters. In [23], from the perspective of virtual impedance, 24 types of single-state feedback AD corresponding to six basic PD strategies are summarised and analysed. It is determined that the capacitor's current feedback strategy of the filter capacitor parallel virtual impedance is the best AD choice, and delay compensation is used to address the effects of the digital delay. To further expand the damping region of the system, He *et al*. [24] proposed an improved method of CCFS, namely the capacitive current proportional–integral feedback strategy (CCPIFS), which successfully raised the upper limit of the system damping region to $0.48f_s$. However, since this method adds a feedback path, the stability margin of the system is insufficient, and it is easy to oscillate during operation. Usually, a PD strategy is needed to ensure a stable system operation.

Considering that fractional-order controllers have more fine-grained control performance than integer-order controllers [24, 25], this paper proposes a new improved method of CCFS, namely capacitive current fractional-order proportional–integral (PI) feedback strategy, which can expand the damping domain of the system. The contributions of this study include the following points:

i. An end-to-end efficient PI feedback framework based on capacitive current fractional-order, dubbed capacitive current fractional PI feedback strategy (CCFPIFS), is carried out, which integrates a single-phase LCL grid-connected inverter and a CCFPIFS-based AD control strategy.
ii. Through the optimal selection of the parameters, the upper limit of the system damping region is very close to the Nyquist frequency increasing the degree of freedom of the system, and thus the system can be controlled more precisely.
iii. The robustness and output power quality of the system are both improved, the stability constraint conditions and simulation experimental results are provided analysed. In addition, the Appendix provides some Bode diagrams and corresponding analyses of the various states that may exist for a dual-current loop system with CCFPIFS.

This paper is arranged as follows: in Section 2, a digitally controlled LCL-type grid-connected inverter system model using CCFS AD and grid-side current single-loop control is established. The problems in the damping region of the system are obtained by analysing the mathematical model of the CCFS virtual equivalent impedance. In Section 3, the CCFPIFS AD control strategy is proposed through the analysis of the virtual equivalent impedance mathematical model of CCFPIFS, the damping range of the system and the stability constraints of the fractional-order PI (FOPI) controller parameters are discussed. Section 4 validates the proposed method through Simulink simulation experiments. The results prove the validity of the theoretical analysis. The difference in control performance between CCFPIFS and other control strategies is compared. Section 5 is the conclusion of this paper.

2 Analysis of LCL grid-connected inverter system based on CCFS

2.1 Structure description of LCL grid-connected inverter system

The system structure of the single-phase LCL grid-connected inverter is shown in Fig. 1, the system adopts double closed-loop feedback control of grid-side current and capacitive current, VT1–VT4 are the switching tubes of the full-bridge inverter. L_1, C, and L_2 form an LCL type filter connected to inverter. v_{in} and v_g represent the DC input voltage and the grid-side voltage, respectively. The grid impedance at the point of common coupling (PCC) is composed of inductance and resistance, since the grid resistance provides damping and helps stabilise the system, it is considered here that the pure inductance L_g represents the worst case. A phase-locked loop (PLL) is used to extract the phase angle at v_{PCC}, and the reference value of the grid-connected current is denoted as $I*$. G_i stands for the current regulator. H_{i1} and H_{i2} are the sampling coefficients of capacitor current i_c and grid-side current i_2.

2.2 Mathematical model of LCL grid-connected inverter system with CCFS

The control block diagram of the system is shown in Fig. 2. $K_{pwm} = v_{in}/v_{tri}$ (v_{tri} is the triangular carrier amplitude) is the transfer function of the inverter bridge. $G_d(s)$ includes 0.5 beat of calculating the delay and 1 beat of the pwm modulation delay, and T_s is the sampling period. $G_d(s)$ can be expressed as

$$G_{\mathrm{d}}(s) \simeq e^{-1.5sT_{\mathrm{s}}}. \tag{1}$$

The current regulator uses a proportional resonance (PR) regulator, and its transfer function is

$$G_i(s) = K_{\mathrm{p}} + \frac{2K_{\mathrm{r}}\omega_i s}{s^2 + 2\omega_i s + \omega_o^2}. \tag{2}$$

where K_{p} is the proportionality coefficient, K_{r} is the resonance gain, $\omega_o = 2\pi f_o$ is the fundamental angular frequency, and ω_i is the bandwidth of the resonance section. The open-loop transfer function $G(s)$ of the system can be obtained from Fig. 2

$$G(s) = \frac{H_{i2}G_i(s)}{sL_1(L_2+L_{\mathrm{g}})C} \cdot \frac{K_{\mathrm{pwm}}G_{\mathrm{d}}(s)}{s^2 + s \cdot H_{i1}K_{\mathrm{pwm}}G_{\mathrm{d}}(s)/L_1 + \omega_{\mathrm{r}}^2}. \tag{3}$$

where ω_{r} is the resonant angular frequency of the LCL filter, and f_{r} stands for resonant frequency:

$$\omega_{\mathrm{r}} = 2\pi f_{\mathrm{r}} = \sqrt{\frac{L_1 + L_2 + L_{\mathrm{g}}}{L_1(L_2+L_{\mathrm{g}})C}}. \tag{4}$$

Formula (4) shows that the factors affecting the resonance frequency include filter parameters L_1, C, L_2, and grid impedance L_{g}.

2.3 Virtual impedance analysis in CCFS

According to the system control block diagram and equivalent physical model diagram in Fig. 2, the current feedback loop of C can be equivalent to a virtual equivalent impedance Z_{eq} in parallel with C. The Z_{eq} can be expressed as

$$Z_{\mathrm{eq}}(s) = \frac{M}{H_{i1}} \cdot \frac{1}{G_{\mathrm{d}}(s)}. \tag{5}$$

where $M = L_1/(K_{\mathrm{pwm}}C)$. Substituting $s = j\omega$, $G_{\mathrm{d}}(s) = e^{-j1.5\omega T_{\mathrm{s}}} = \cos 1.5\omega T_{\mathrm{s}} - j\sin 1.5\omega T_{\mathrm{s}}$ into formula (5) can yield

$$\begin{aligned} \frac{1}{Z_{\mathrm{eq}}}(\omega) &\triangleq \frac{1}{R_{\mathrm{eq}}(\omega)} + \frac{1}{jX_{\mathrm{eq}}(\omega)} \\ &= \frac{H_{i1}}{M}(\cos 1.5\omega T_{\mathrm{s}} - j\sin 1.5\omega T_{\mathrm{s}}). \end{aligned} \tag{6}$$

It can be seen from formula (6) that Z_{eq} can be expressed as a virtual resistance R_{eq} in parallel with a virtual reactance X_{eq}, the mathematical models of R_{eq} and X_{eq} can be expressed as

$$\begin{aligned} R_{\mathrm{eq}}(\omega) &= \frac{M}{H_{i1}} \cdot \frac{1}{\cos\theta} \\ X_{\mathrm{eq}}(\omega) &= \frac{M}{H_{i1}} \cdot \frac{1}{\sin\theta}. \end{aligned} \tag{7}$$

where $\theta = 1.5\omega T_{\mathrm{s}} = 1.5\omega/f_{\mathrm{s}}$, f_{s} is the sampling frequency. According to formula (7), the frequency characteristics of R_{eq} and X_{eq} can be drawn as shown in Fig. 3.

Based on the analysis of Figs. 2*b* and 3, it can be seen that the main function of X_{eq} is to be in parallel with the C in the LCL filter, thus affecting ω_{r}, which is reflected in formula (4). When $H_{i1} > 0$, $|X_{\mathrm{eq}}| > 0$ in $(0, f_{\mathrm{s}}/3)$ and $|X_{\mathrm{eq}}| < 0$ in $(f_{\mathrm{s}}/3, f_{\mathrm{s}}/2)$, since the filter capacitor C is parallel to the X_{eq}, it can be seen from formula (4), $f_{\mathrm{r}}' > f_{\mathrm{r}}$ in $(0, f_{\mathrm{s}}/3)$, and $f_{\mathrm{r}}' < f_{\mathrm{r}}$ in $(f_{\mathrm{s}}/3, f_{\mathrm{s}}/2)$, where f_{r}' is the actual resonant frequency, it is affected by CCFS and L_{g}.

The main function of R_{eq} is to affect the stability of the system. The damping domain of the system can be judged according to the

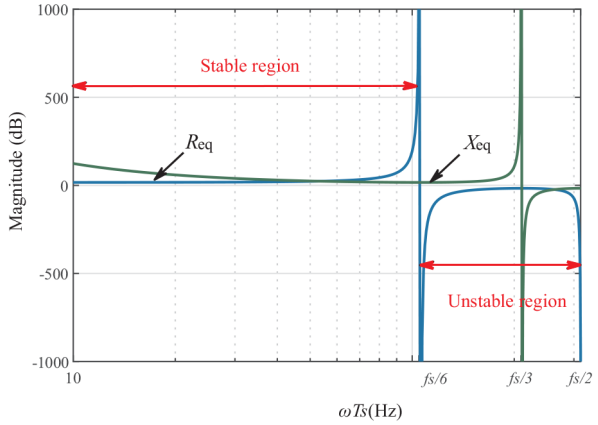

Fig. 3 *At $H_{i1} > 0$, the frequency characteristics of R_{eq} and X_{eq}*

$|R_{\mathrm{eq}}|$. When $H_{i1} > 0$, $|R_{\mathrm{eq}}| > 0$ in $(0, f_{\mathrm{s}}/6)$ and $|R_{\mathrm{eq}}| < 0$ in $(f_{\mathrm{s}}/6, f_{\mathrm{s}}/2)$, since $|R_{\mathrm{eq}}| > 0$ can damp the resonance peak of the system, the system is stable in $(0, f_{\mathrm{s}}/6)$, while $|R_{\mathrm{eq}}| < 0$ will introduce two poles of the right-half plane of the s-domain, at which point the system is unstable in $(f_{\mathrm{s}}/6, f_{\mathrm{s}}/2)$. Taking $\omega = 2\pi f$ into account, f is the frequency of the system, the critical conditions for system stability and the critical stability frequency are shown below

$$\begin{aligned} R_{\mathrm{eq}}(\omega) &= \frac{M}{H_{i1}} \cdot \frac{1}{\cos\theta} = \pm\infty. \\ f &= \frac{kf_{\mathrm{s}}}{3} + \frac{f_{\mathrm{s}}}{6}, \quad k \in N. \end{aligned} \tag{8}$$

Based on the above analysis, $H_{i1} > 0$, the system is unstable when $f_{\mathrm{r}}' \in (f_{\mathrm{s}}/6, f_{\mathrm{s}}/2)$. By the same analytical method, $H_{i1} < 0$, the system is unstable when $f_{\mathrm{r}}' \in (0, f_{\mathrm{s}}/6)$. Although f_{r} can be determined by designing filter parameters L_1, C and L_2, due to the influence of X_{eq} and L_{g}, there is a certain deviation between f_{r} and f_{r}'. Hence, a suitable damping method is needed to expand the damping domain of the system and providing better system stability.

Remark 1: Generally, the controllability of the system is usually ensured in $f_{\mathrm{r}}' < f_{\mathrm{s}}/2$, but $f_{\mathrm{r}}' > f_{\mathrm{s}}/2$ may exist when $H_{i1} < 0$. In this study, this issue is not considered.

3 Analysis of LCL grid-connected inverter system based on CCFPIFS

To ensure the stable operation of the system with the influence of X_{eq} and L_{g}, we expand the positive frequency range of equivalent virtual resistance. The new scheme proposed in this paper is to change the proportional feedback loop of the capacitor current into a proportional-fractional–integral feedback loop. Based on the CCFS and CCPIFS, the precise control characteristics of the fractional-order controller are utilised to obtain a better damping effect.

3.1 Mathematical model of the system with CCFPIFS

Fig. 4 shows the system control model of CCFPIFS. According to Fig. 4*a*, CCFPIFS adds a fractional integral feedback loop of the capacitor current on the basis of CCFS. It can be considered that the capacitor current feedback loop changes from the proportional feedback loop to the FOPI controller feedback loop. Since the right half-plane zero is introduced when the FOPI controller coefficients are reversed, only the condition of $H_{i1}/K > 0$ is considered, where K represents the feedback coefficient of the fractional–integral loop. The additional equivalent virtual impedance Z_{foi} is reflected in the physical model of Fig. 4*b*, which is in parallel with C and Z_{eq}. To analyse the equivalent virtual impedance of CCFPIFS, this

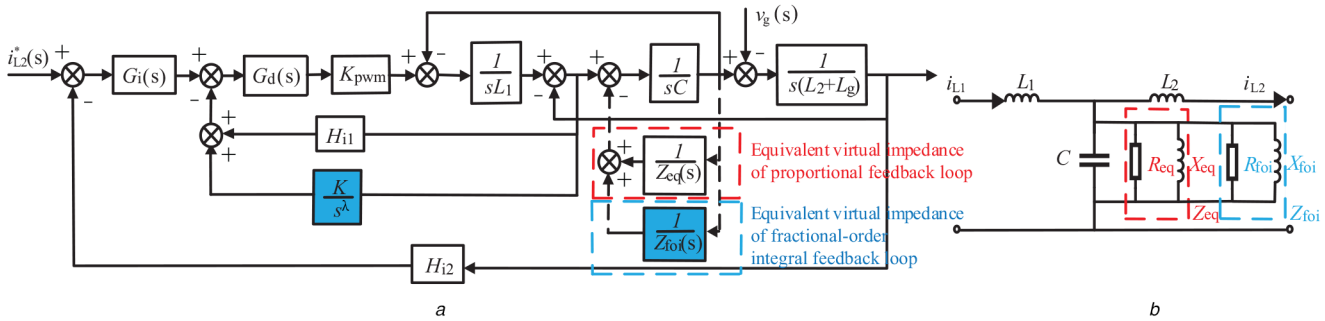

Fig. 4 *System model with CCFPIFS*
(a) System control block diagram, ***(b)*** Equivalent circuit diagram

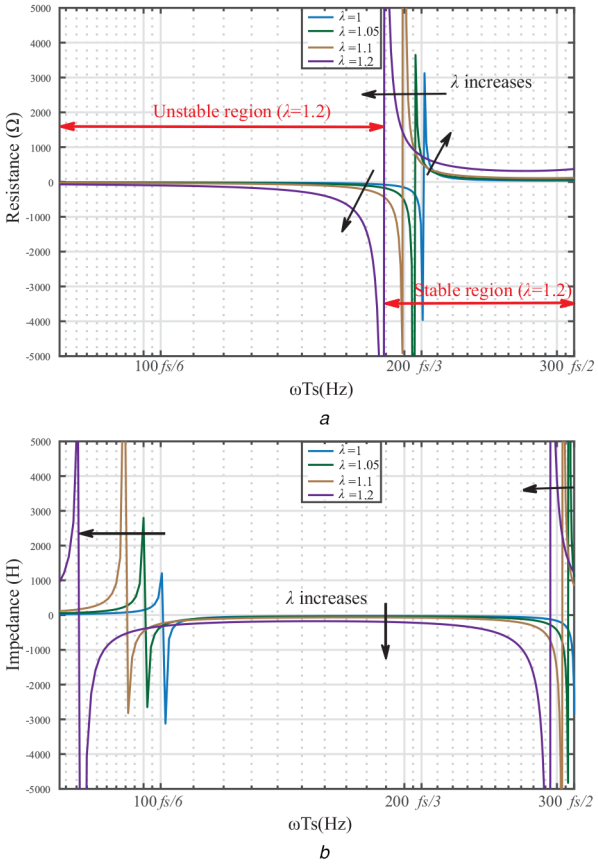

Fig. 5 *At $K > 0$, frequency characteristic of R_{foi} and X_{foi}*
(a) R_{foi} model, ***(b)*** X_{foi} model

paper considers that $Z_{fopi}(\omega) = Z_{eq}(\omega)Z_{foi}(\omega)$. According to Fig. 4, the transfer function of the system with CCFPIFS is

$$G_2(s) = \frac{H_{i2}G_i(s)}{sL_1(L_2+L_g)C} \times \frac{K_{pwm}G_d(s)}{s^2 + s\cdot G_{fopi}(s)K_{pwm}G_d(s)/L_1 + \omega_r^2}. \tag{9}$$

where $G_{fopi}(s)$ represents the FOPI controller in the capacitor current FOPI feedback loop, λ is the fractional order of the integral, and its value is in the range of (0, 2). The transfer function of $G_{fopi}(s)$ is shown in formula (10)

$$G_{fopi}(s) = (H_{i1} + K/s^\lambda). \tag{10}$$

According to Fig. 4*b*, $Z_{fopi}(\omega)$ can be subdivided as follows:

$$\begin{aligned}\frac{1}{Z_{fopi}} &= \frac{1}{R_{fopi}} + \frac{1}{jX_{fopi}} \triangleq \frac{1}{Z_{eq}} + \frac{1}{Z_{foi}} \\ &\triangleq \frac{1}{R_{eq}} + \frac{1}{R_{foi}} + \left(\frac{1}{jX_{eq}} + \frac{1}{jX_{foi}}\right)\end{aligned} \tag{11}$$

The equivalent virtual impedance of Z_{foi} can be expressed as

$$Z_{foi}(s) = \frac{s^\lambda M}{Ke^{-1.5sT_s}}. \tag{12}$$

Considering the substitution of $s = j\omega$ and $j^\lambda = e^{j(\lambda\pi/2)}$, the Z_{foi} can be solved as

$$\begin{aligned}\frac{1}{Z_{foi}(\omega)} &\triangleq \frac{1}{R_{foi}(\omega)} + \frac{1}{jX_{foi}(\omega)} \\ &= \frac{K}{\omega^\lambda M}\cdot(\cos(\theta+\theta_\lambda) - j\sin(\theta+\theta_\lambda)).\end{aligned} \tag{13}$$

where $\theta_\lambda = \lambda\pi/2$. According to formula (13), the expressions of R_{foi} and X_{foi} are as follows:

$$\begin{aligned}R_{foi}(\omega) &= \frac{\omega^\lambda\cdot M}{K}\cdot\frac{1}{\cos(\theta+\theta_\lambda)}. \\ X_{foi}(\omega) &= \frac{\omega^\lambda\cdot M}{K}\cdot\frac{1}{\sin(\theta+\theta_\lambda)}.\end{aligned} \tag{14}$$

The same as formula (8), the critical stability condition of the fractional–integral feedback loop is

$$\begin{aligned}R_{foi}(\omega) &= \frac{\omega^\lambda\cdot M}{K}\cdot\frac{1}{\cos(\theta+\theta_\lambda)} = \pm\infty. \\ f &= \frac{kf_s}{3} + \frac{(1-\lambda)f_s}{6}, \quad k\in N.\end{aligned} \tag{15}$$

According to formulae (14) and (15), the frequency characteristics of R_{foi} and X_{foi} under different λ conditions can be drawn separately in Fig. 5. It can be seen from Fig. 5 that when $K > 0$ and $\lambda \geq 1$, $|R_{foi}| < 0$ in $(0, (3-\lambda)/6\cdot f_s)$ and $|R_{foi}| > 0$ in $((3-\lambda)/6\cdot f_s, f_s/2)$. With the λ increases, the stable region of $|R_{foi}| > 0$ gets bigger. $|X_{foi}| > 0$ in $(0, (2-\lambda)/6\cdot f_s)$ and $((4-\lambda)/6\cdot f_s, f_s/2)$, and $|X_{foi}| < 0$ in $((2-\lambda)/6\cdot f_s, (4-\lambda)/6\cdot f_s)$. As the λ increases, the region of $|X_{foi}| > 0$ is significantly reduced.

When $\lambda < 1$, it can be seen in the following discussion, the region of $|R_{foi}| > 0$ is changing, but the region length is not significantly changed, the stability of the system is also weakened, so it is not considered.

3.2 Characteristic analysis of CCFPIFS equivalent virtual impedance

According to the equivalent physical model of CCFPIFS in Fig. 4*b*, it can be seen that $R_{fopi}(\omega) = R_{eq}(\omega)//R_{foi}(\omega)$, and

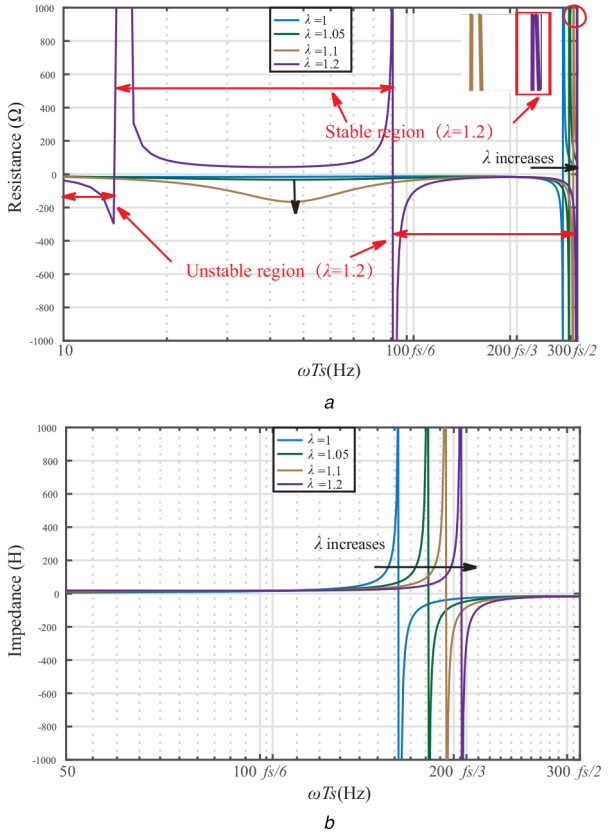

Fig. 6 *At $H_{i1} > 0$ and $K > 0$, frequency characteristic of R_{fopi} and X_{fopi}*
(a) *R_{fopi} model,* ***(b)*** *X_{fopi} model*

Table 1 Frequency domain range of system virtual impedance under different feedback paths

Case	$\lvert Z\rvert > 0$	$\lvert Z\rvert < 0$
R_{eq}	$(0, f_s/6)$	$(f_s/6, f_s/2)$
R_{foi}	$((3-\lambda)/6 \cdot f_s, f_s/2)$	$(0, (3-\lambda)/6 \cdot f_s)$
R_{fopi}	$(A, f_s/2)$	$(0, A)$
X_{eq}	$(0, f_s/3)$	$(f_s/3, f_s/2)$
X_{foi}	$(0, (2-\lambda)/6 \cdot f_s)$ & $((4-\lambda)/6 \cdot f_s, f_s/2)$	$((2-\lambda)/6 \cdot f_s, (4-\lambda)/6 \cdot f_s)$
X_{fopi}	$(0, B)$	$(B, f_s/2)$

Discuss case under $H_{i1} > 0$ and $K > 0$. The parameters in the table are $A = (f_s/6\pi) \cdot \arccos(1 - (3K/H_{i1}f_s))$ and $B = (f_s/6\pi) \cdot \arccos(1 - (2K/H_{i1}))$.

$X_{\text{fopi}}(\omega) = X_{\text{eq}}(\omega)//X_{\text{foi}}(\omega)$. Therefore, substituting formulae (7) and (14) into formula (12), $R_{\text{fopi}}(s)$ and $X_{\text{fopi}}(s)$ of the CCFPIFS can be obtained as follows:

$$\begin{aligned} R_{\text{fopi}}(\omega) &= \cdot \frac{M\omega^{\lambda}}{K \cdot \cos(\theta + \theta_{\lambda}) + \omega^{\lambda} H_{i1} \cos\theta}. \\ X_{\text{fopi}}(\omega) &= \cdot \frac{M\omega^{\lambda}}{K \cdot \sin(\theta + \theta_{\lambda}) + \omega^{\lambda} H_{i1} \sin\theta}. \end{aligned} \tag{16}$$

When $H_{i1} > 0$ and $K > 0$, the frequency characteristics of R_{fopi} and X_{fopi} under different λ conditions can be drawn separately in Fig. 6. As shown in Fig. 6*a*, with the fractional order λ increases, the range of $\lvert R_{\text{fopi}}\rvert < 0$ gets bigger. However, when λ is greater than a certain degree, such as $\lambda \geq 1.2$ in Fig. 6*a*, $\lvert R_{\text{fopi}}\rvert$ has a section of opposite amplitude in the low-frequency band, there are situations where $\lvert R_{\text{fopi}}\rvert > 0$ and $\lvert R_{\text{fopi}}\rvert < 0$. From Fig. 6*b*, with λ increases, the range of $\lvert X_{\text{fopi}}\rvert > 0$ gets bigger. Considering that the composition of the X_{fopi} interval is relatively simple, the relationship between f_r' and f_r can be roughly judged by Fig. 6*b*, and the specific coefficient relationship can be obtained by formulae (4) and (16).

It can be seen from formula (16) that $M > 0$, $\omega > 0$, $\lvert R_{\text{fopi}}\rvert$, and $\lvert X_{\text{fopi}}\rvert$ are plus or minus depending on H_{i1} and K. When $K < 0$ and $H_{i1} < 0$, the frequency characteristics of R_{fopi} and X_{fopi} are mirror images of Fig. 6, and the critical conditions are the same. With the λ increases, the range of $\lvert R_{\text{fopi}}\rvert > 0$ gets bigger. It can be seen from the above discussion, when $K < 0$ and $H_{i1} < 0$, the maximum damping domain can be obtained.

To ensure the stable operation of the system, the range of $\lvert R_{\text{fopi}}\rvert > 0$ needs to be as large as possible, since the system has to satisfy the condition that $H_{i1}/K > 0$, the feedback loop parameters are selected as $K < 0$ and $H_{i1} < 0$.

Since $K < 0$ and $H_{i1} < 0$, the critical condition of R_{fopi} and X_{fopi} do not change, the critical condition of R_{fopi} reflects the critical damping frequency of the system using CCFPIFS, and the critical conditions of X_{fopi} reflect the offset direction of f_r'. The critical conditions of $\lvert R_{\text{fopi}}\rvert$ and $\lvert X_{\text{fopi}}\rvert$ are shown below

$$\begin{aligned} &R_{\text{fopi}}(\omega) = \pm\infty, \quad X_{\text{fopi}}(\omega) = \pm\infty. \\ &K \cdot \cos(\theta + \theta_{\lambda}) + \omega^{\lambda} H_{i1} \cos\theta = 0. \\ &K \cdot \sin(\theta + \theta_{\lambda}) + \omega^{\lambda} H_{i1} \sin\theta = 0 \end{aligned} \tag{17}$$

Since formula (17) is a transcendental equation, the approximate solution is given and discussed in this section, and the detailed analytic process will be given in the next section. To ensure the maximum damping interval, $1 < \lambda < 1.2$ is chosen in this paper. Then substituting the approximate conditions that $\omega^{\lambda} = \omega$ and $\sin(\lambda\pi/2) = 1$ into formula (17), and the approximate expression of formula (17) can be obtained as follows:

$$\begin{aligned} &K\cos\frac{\lambda\pi}{2} - K\tan\frac{3}{2}\omega T_s + \omega H_{i1} = 0. \\ &K\tan\frac{3}{2}\omega T_s \cdot \cos\frac{\lambda\pi}{2} + K + \omega H_{i1}\tan\frac{3}{2}\omega T_s = 0. \end{aligned} \tag{18}$$

The approximate solution of the critical frequency can be obtained by the derivative treatment of formula (18), and then combined with formulae (6), (7), (14), and (15). The frequency-domain range of the virtual impedance is shown in Table 1.

Comparing the FOPI controller feedback link with the proportional feedback link and fractional-integral feedback link in Table 1, the virtual resistance frequency interval of $\lvert Z\rvert < 0$ changes from $R_{\text{eq}} \in (f_s/6, f_s/2)$ to $R_{\text{fopi}} \in (0, A)$, as the λ increases, the negative interval increases and is close to $R_{\text{fopi}} \in (0, f_s/2)$. The $\lvert Z\rvert > 0$ damping region is converted from $R_{\text{eq}} \in (0, f_s/6)$ to $R_{\text{fopi}} \in (A, f_s/2)$, the positive damping region decreases significantly and is close to 0 with λ increases, but when λ is too large, R_{fopi} has a positive interval in the low-frequency band. The virtual reactance frequency region of $\lvert Z\rvert < 0$ changes from $X_{\text{eq}} \in (f_s/3, f_s/2)$ to $X_{\text{fopi}} \in (B, f_s/2)$, and the equivalent virtual impedance is capacitive at this time, the equivalent filtering capacitor $C' > C$, the resonant frequency $f_r' < f_r$. $\lvert Z\rvert > 0$ region is changed from $X_{\text{eq}} \in (0, f_s/3)$ to $X_{\text{fopi}} \in (0, B)$, and the equivalent virtual impedance is inductive, $C' > C$, $f_r' < f_r$. The situation is the same for $H_{i1} < 0$ and $K < 0$.

Remark 2: To further analyse the damping effect of CCFPIFS, all possible cases of the system under difference L_g are given in Table 2, and the system Bode diagram and correlation analysis are given in the Appendix.

3.3 FOPI controller parameter characteristics analysis

According to the above analysis, to ensure the stability of the system, the constraints of the CCFPIFS system can be given from formula (19) that

$$K \cdot \cos(\theta + \theta_\lambda) + \omega^\lambda H_{i1} \cos\theta > 0. \quad (19)$$

in which, $K < 0$ and $H_{i1} < 0$.

Since there are four variables in formula (19), which is not convenient for further analysis of the stability conditions of the system, formula (18) is adjusted to become three variables H_{i1}/K, ωT_s, and λ. At this point, 3D images can be drawn through the Mupad toolbox of MATLAB, but it is still difficult to analyse. Furthermore, three 2D images are drawn, respectively, as Figs. 7–9, and the stability constraints of the system are discussed further.

Table 2 Stability analysis of LCL grid-connected inverter with CCFPIFS

Case	λ	The number of 0 dB points	Phase angle jump at f_r'	Gain margin	Phase margin	Stability judgment
1	< 1	1	↓	—	—	unstable
2	1	1	↓	GM > 0	PM > 0	stable
3	> 1	1	↓	GM > 0	PM > 0	stable
4	> 1	3	↓	—	—	unstable
5	> 1	3	↑	GM > 0	PM > 0	stable
6	> 1	1	↑	—	PM > 0	stable

Discuss case under that: λ meets the constraints, $H_{i1} < 0$ and $K < 0$.

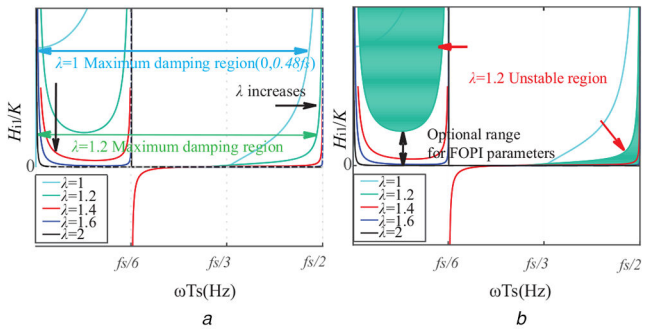

Fig. 7 *Frequency characteristic curve of H_{i1}/K*

(a) Diagram of H_{i1}/K and ωT_s, ***(b)*** Diagram of system stability domain when λ is determined

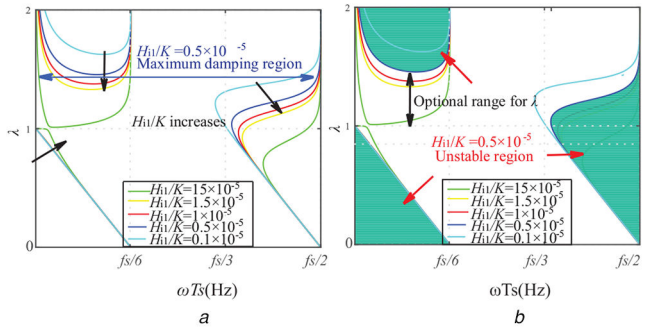

Fig. 8 *Frequency characteristic curve of λ*

(a) Diagram of λ and ωT_s, ***(b)*** Diagram of system stability domain when H_{i1}/K is determined

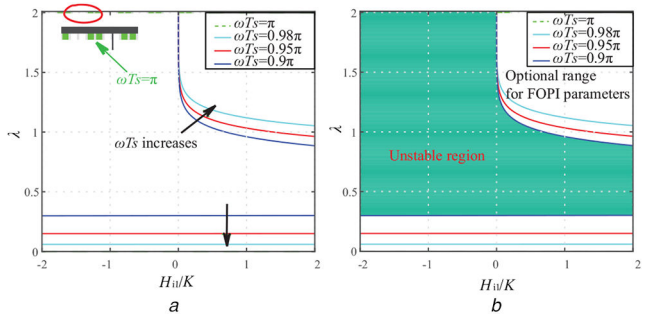

Fig. 9 *Parameter characteristic curve of λ*

(a) Diagram of λ and H_{i1}/K, ***(b)*** Diagram of system stability domain when ωT_s is determined

(i) When λ is determined, the relationship between H_{i1}/K and ωT_s: from Fig. 7*a*, when $\lambda = 1$, the maximum damping region is $(0, 0.48 f_s)$, and as the λ increases, the maximum damping region keeps expanding, but correspondingly, the selection range of parameter H_{i1}/K is narrowed. The green shaded region in Fig. 7*b* is the unstable region corresponding to $\lambda = 1.2$, when the point corresponding to the resonant frequency and H_{i1}/K is located in the region, the system cannot run stably.

Following the above analysis, we observe that (i) when a certain parameter λ is determined, the larger the value of H_{i1}/K within the constraint range, the larger the system damping region, but when H_{i1}/K exceeds the constraint range, the unstable region appears at low frequencies; (ii) the larger λ, the wider the system damping region range, but the constraint conditions of the corresponding coefficient H_{i1}/K is stricter; (iii) it can be seen that when $\lambda = 2$, the system can take the damping region as $(0, f_s/2)$, but H_{i1}/K does not have an effective solution. Hence, it can be obtained that this method can approach a constant stable system infinitely.

(ii) When H_{i1}/K is determined, the relationship between λ and ωT_s: from Fig. 8*a*, as the H_{i1}/K increases, the maximum damping region keeps expanding, but correspondingly, the selection range of λ is narrow. The green shaded region in Fig. 8*b* is the unstable region corresponding to $H_{i1}/K = 0.5 \times 10^{-5}$, when the point corresponding to the resonant frequency and λ is located in the region, the system cannot run stably.

Following the above analysis, we observe that: (i) under a certain H_{i1}/K, when $\lambda > 1$, the larger the λ when the constraint conditions are satisfied, the larger the system damping domain, but when λ exceeds the constraint range, the unstable region appears at low frequencies; (ii) when H_{i1}/K is reduced, the upper limit of the system damping domain increases, but the corresponding λ is increased accordingly; (iii) when $0 < \lambda < 1$, with the λ increases, the starting point for positive virtual resistance is shifted from $f_s/6$ to 0, but the region length is not significantly changed. Therefore, the case of $0 < \lambda < 1$ is not considered in this paper.

(iii) When ωT_s is determined, the relationship between λ and H_{i1}/K, there are the green shaded region in Fig. 9*b* is the unstable region when $\omega T_s = 0.9\pi$, and the upper limit of the damping domain is $\omega T_s/2\pi = 0.45 f_s$. The line corresponds to the relationship of parameters when the system is critically stable. It can be seen from Fig. 9 that with the expansion of the upper limit of the damping region, the select range of the parameters H_{i1}/K and λ gradually decreases. When the upper limit of the damping domain is $0.5 f_s$, there is no valid parameter select range.

Through the aforementioned analysis, there are according to the above analysis, it can be seen that the constraint conditions of λ are: $1 < \lambda < 2$ and the constraint range of Fig. 9 must be satisfied when H_{i1}/K is determined. The constraint conditions of H_{i1}/K are $H_{i1} < 0$, $H_{i1}/K > 0$, and the constraint range of Fig. 8 must be satisfied when λ is determined. Fig. 9 presents the selection range of H_{i1}/K and λ when the upper limit of the damping region is determined. The FOPI controller parameter design can be performed based on the above analysis.

4 Experimental results and analysis

4.1 Root locus analysis of systems using CCFPIFS

Figs. 10*a* and *b* show the distribution of the closed-loop zero poles of the system, respectively. Since the stability of the system is mainly affected by the closed-loop poles, so the effects of closed-loop zero and dipole are not considered for the time being. It can be seen from Fig. 11*a*, when $\lambda \simeq 1$, the system is difficult to run stably, and with the increase of λ, the system gradually changes from unstable to stable, and then finally outside the unit circle. The

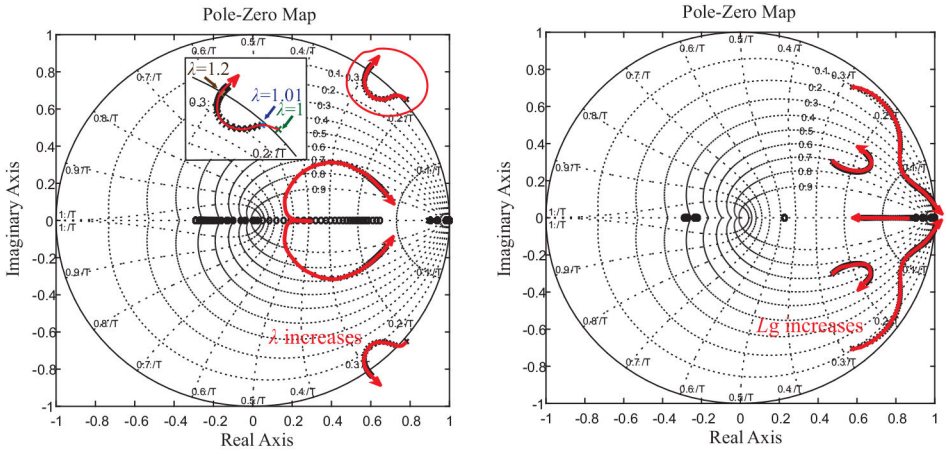

a b

Fig. 10 *Distribution of closed-loop zero poles of CCFPIFS system*

(a) Distribution of closed loop zero poles when λ changes, ***(b)*** Distribution of closed loop zero poles when L_g changes

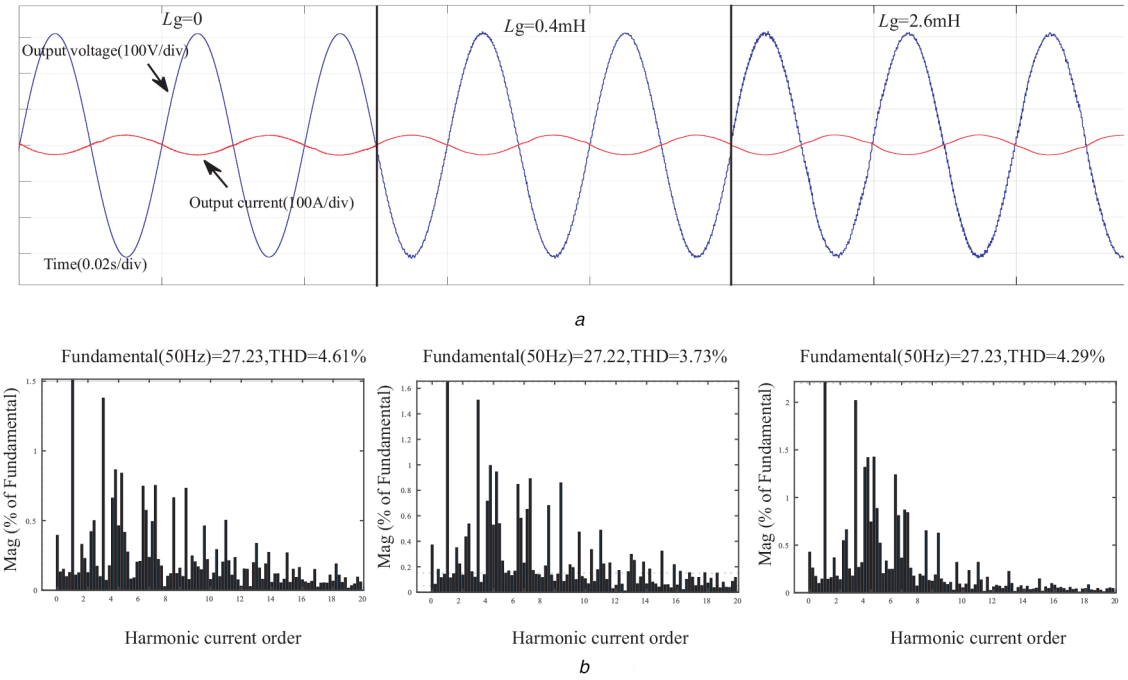

a b

Fig. 11 *Output power quality waveform of the system under different grid impedances*

(a) Waveform of the output voltage and current of the system, ***(b)*** Output current total harmonic distortion (THD) analysis as $L_g = 0$, $L_g = 0.4$mH, $L_g = 2.6$mH

Table 3 System parameter table

Parameter	Symbol	Value	Parameter	Symbol	Value
input voltage	v_{in}	360 V	inverter-side inductor	L_1	0.9 mH
grid voltage	v_g	220 V	grid-side inductor	L_2	0.4 mH
output power	P_{out}	6 kW	filter capacitor	C	10 μF
fundamental frequency	f_o	50 Hz	switching frequency	f_{sw}	10 kHz
sampling frequency	f_s	15 kHz	grid-side current feedback coefficient	H_{i2}	0.15
triangle carrier	v_{tri}	5 V	LCL	f_r	3.6 kHz
internal resistance of DC	R_{in}	0.1 Ω	bandwidth of PR controller	ω_i	0.1π

system has a certain stability range, which is consistent with the conclusion of the system stability constraints in Section 3. Fig. 11*b* shows that as L_g varies, the closed-loop poles of the system with CCFPIFS are basically distributed in the unit circle, and the system can ensure stable operation. Therefore, compared with CCPIFS, CCFPIFS has better stability, and can still guarantee the stable operation of the system when the strong grid becomes the weak grid, CCFPIFS has strong robustness.

4.2 Analysis of simulation results

To verify the feasibility of the proposed method, a 6 kW single-phase LCL grid-connected inverter model was built in Matlab Simulink. The specific parameters of the model are shown in Table 3. The parameters of the FOPI controller are $H_{i1} = -0.06$, $K = -1600$, and $\lambda = 1.19$. For the PR controller, when PM = 60° and $f_c \simeq 4\% f_s$, the method proposed in the literature [26] and the simulation adjustment method were adopted, and $K_p = 0.5$ and $K_r = 1200$ was selected to meet THD requirements. Moreover, to simulate the actual state, $I*$ is enabled at 0.04 s.

Remark 3: The parameter design process of the FOPI controller in the control system is as follows: first, considering the situation of the power grid, the range of the stability domain is selected, and select the corresponding parameters range of λ and H_{i1}/K according to Fig. 9, here we assume that the left starting point of

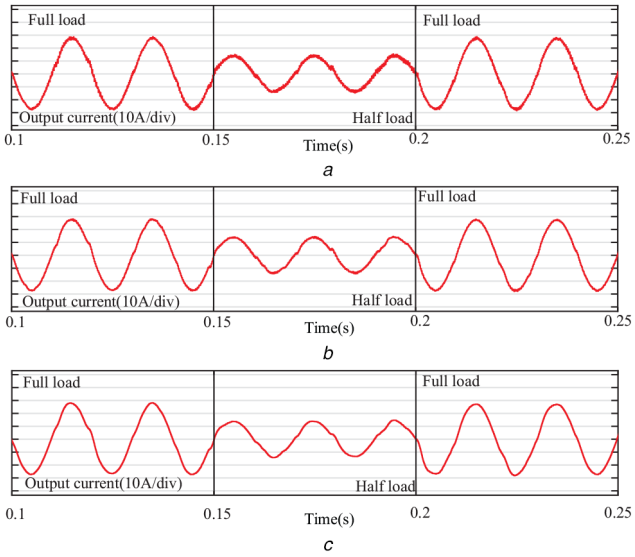

Fig. 12 *Voltage and current waveforms on the grid side of the system when full load and half load are changed*
(a) $L_g = 0$, ***(b)*** $L_g = 0.4$ mH, ***(c)*** $L_g = 2.6$ mH

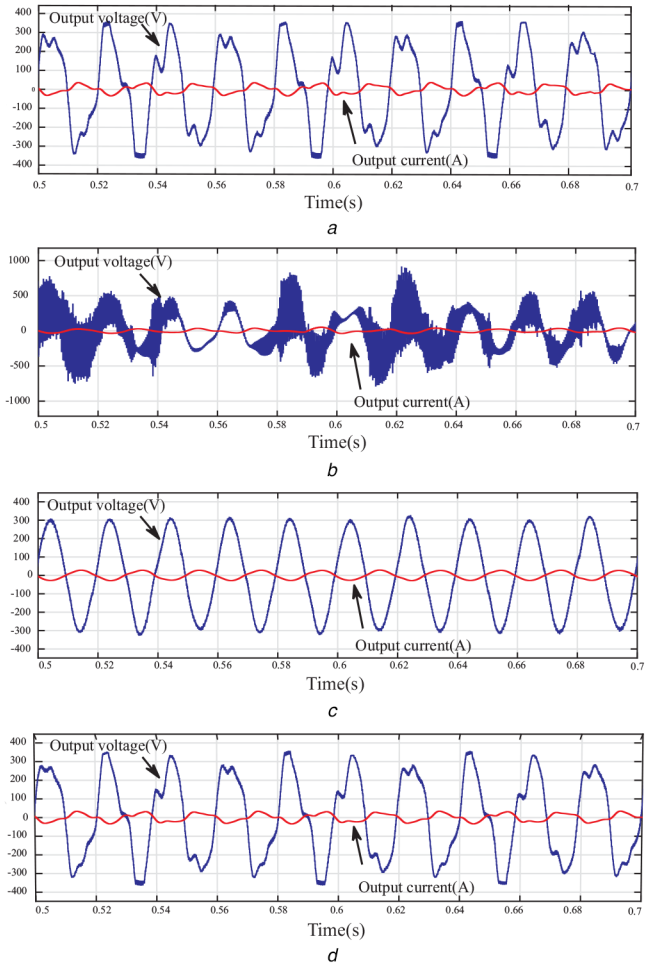

Fig. 13 *Output waveform of the system under different control strategies*
(a) $\lambda = 0$, ***(b)*** $\lambda = 1$, ***(c)*** $\lambda = 1.1$, ***(d)*** $\lambda = 1.2$

the stable region is 0. Then by substituting the range of the stability domain into Fig. 7, multiple groups of λ and H_{i1}/K can be obtained. Finally, the appropriate parameters of the FOPI controller are selected through the system Bode diagram and Simulink test.

Remark 4: In the implementation process, the fractional integration of the capacitor current is prone to problems, such as DC errors and large transient errors, which have a certain impact on the stability and speed of the system. To ensure the stability and speed of the system, the feedback link of the capacitive current is changed from $(H_{i1} + K/s^{\lambda}) \cdot i_c$ to $H_{i1} \cdot i_c + (K/s^{\lambda}) \cdot sC \cdot u_c$.

The implementation steps of the fractional-order PI–derivative controller include discrete and approximation, the approximate process is divided into the direct approximation method and indirect approximation method, respectively, on behalf of the fractional-order controller is realised in the chips or PC. In view of the simulation model provided in this paper, the match method is adopted to discretise the fractional-order-integral link. The approximate method of the controller is the indirect approximation method of refined Oustaloup, the approximate frequency band is (0.001, 1000), and the approximate order is selected as the fifth order.

The waveform and THD analysis of the output voltage and current are shown in Fig. 11. The blue line in Fig. 11*a* is the output voltage, and the red line is the output current. When $L_g = 0$, $L_g = 0.4$mH and $L_g = 2.6$mH, the system works in the inverter state, and maintains the unit power factor state. Fig. 11*b* shows the THD analysis of output current, when $L_g = 0$, THD = 4.61%, and with the L_g increases, the output power THD decreases monotonically, such as $L_g = 0.4$ mH and THD = 3.73%, better power quality can be achieved. When L_g is large, the input voltage of the PLL has a large distortion, so THD increases when $L_g = 2.6$ mH.

The dynamic performance of the system with CCFPIFS is shown in Fig. 12. The output power of the system changes from 6 kW at full load to 3 kW at half load at 0.15 s, and then changes back to full load at 0.2 s. It can be seen that the output power is adjusted when the current waveform crosses zero, although the slope of the current waveform is the largest at this time, the system current can complete the dynamic adjustment process in a quarter cycle, and the dynamic tracking ability of the system is not significantly changed under the different grid impedance conditions. It can be seen from the above discussion that CCFPIFS has good dynamic performance and strong robustness.

To verify the effectiveness of the constraints proposed in Section 3.3 of this paper, and compare the performance differences of CCFS, CCPIFS, and CCFPIFS, the output voltage and current waveforms of the system at $L_g = 9.6$mH are shown in Fig. 13. Figs. 13*a* and *b* are, respectively, the system output waveforms corresponding to CCFS and CCPIFS, Figs. 13*c* and *d*, respectively, corresponding to the CCFPIFS when $\lambda = 1.1$ and 1.2, at this time $f_r' < f_s/6$. As seen in Fig. 13*a*, under the condition of $L_g = 9.6$ mH, due to the limitation of the damping region, the system based on CCFS cannot maintain stability. From Fig. 13*b*, CCPIFS can be understood as a special case of CCFPIFS when $\lambda = 1.1$, at which time the output voltage and current waveforms

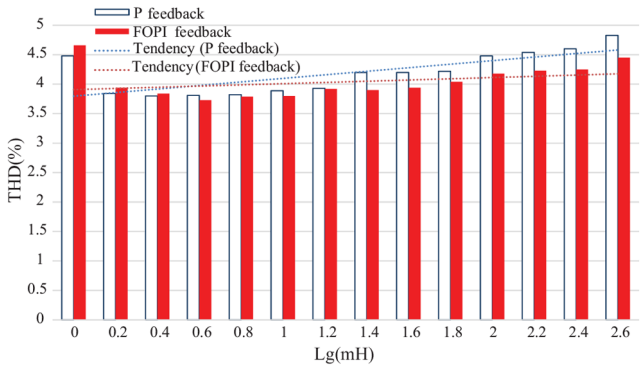

Fig. 14 *System output current quality under different control strategies with L_g changes*

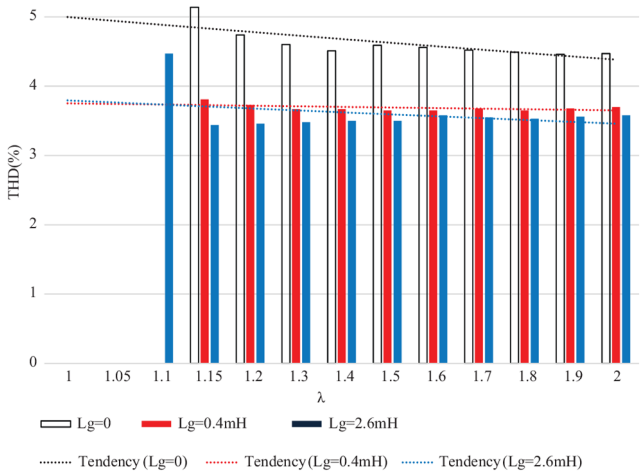

Fig. 15 *System output current quality with λ changes*

are not ideal, and additional PD is required to ensure stable operation of the system, this case is consistent with the conclusion of root trajectory analysis in Fig. 10*a*. It can be known from Fig. 13*c* that when $\lambda = 1.1$, only using CCFPIFS can keep the system stable and work in the state of unit power factor. The output current also conforms to the grid-connected standard. When $\lambda = 1.2$, as is seen from Fig. 13*d*, the system adopting CCFPIFS is in an unstable state. Accordingly there is an upper limit for λ that maintains the system stability, when λ is too large, if ω_r is not appropriate, the system will also be unstable, which consistent with the system stability constraints obtained in Section. 3.3.

To compare THD differences between CCFS and CCFPIFS control strategies, Fig. 14 shows a histogram of the system output current THD with different L_g. When $L_g < 0.4$ mH, the THD of CCFS is slightly lower than CCFPIFS, but the gap between the two is small. As L_g increases, the THD of CCFS and CCFPIFS is reduced to different degrees, and the THD of CCFPIFS decreases faster. When $L_g = 0.4$ mH, both methods have the same output current THD. When $L_g > 0.4$ mH, the THD of CCFS is slightly higher than CCFPIFS, and the larger the L_g, the greater the difference in control effect. According to the analysis in Figs. 13 and 14, the grid-connected power quality of the two damping strategies is close to each other in the case of a strong power network, but in the case of a weak power network, the CCFPIFS has obviously better performance.

Fig. 15 shows a histogram of grid-connected current quality when CCFPIFS is adopted. It can be seen from Fig. 15 that when $\lambda \leq 1.1$, the system cannot operate stably. With the increase of L_g, the system can operate stably when $L_g = 2.6$ mH and $\lambda = 1.1$, it can be seen that when $\lambda \simeq 1$, the stability of the system is relatively poor in the case of small internal resistance of the system, which is consistent with Fig. 13*b*. As λ increases from 1 to 2, the system can still guarantee stable operation, and the THD of the output current does not change much. In contrast, Figs. 15 and 13*d* can be seen

Table 4 Comparison of this method with related methods

Method	[27]	[28]	[29]	Proposed method
observed signals	inverter-side current, grid-side current, capacitor voltage	inverter-side current	output power	grid-side current, capacitor current and voltage
control method	generalised droop control	generalised predictive control, finite impulse response filter	static output feedback control	PR controller, FOPI controller
degrees of freedom and complexity	medium	high	high	medium
reaction speed	second	millisecond	second	millisecond
high tolerance parameter	frequency and output power	LCL filter parameters	frequency fluctuation	grid impedance

that when $\lambda = 1.2$, the system with $L_g = 2.6$ mH can run stably, but the system with $L_g = 9.6$ mH cannot, which corresponds to what Fig. 6*a* shows. The system exists negative damping in the low-frequency domain, so the size of the L_g decides the size of f_r'. It can be concluded that under strong grid conditions, the system stability constraints of λ are relatively loose, and the performance is better than CCFS. However, if the stability of the whole sampling frequency range is taken into account, the system still needs to meet the stability constraints given in Section 3.3.

4.3 Analysis of advanced inverter control strategies

The performance comparison between the control method proposed in this paper and several advanced inverter system control strategies are shown in Table 4. The following control characteristics are considered: observed signals, control methods, degrees of freedom and complexity, and high tolerance parameters of the system. Among them, the observed signals reflect the number of sensors in the system, the degree of freedom of the control quantity reflects the complexity of the control strategy, the reaction speed represents how fast the system responds to changes in load, and the high tolerance parameters represent the biased aspects of the high robustness system in Table 4. It can be seen that several kinds of systems have different preferences and advantages in different aspects.

5 Conclusion

This paper introduces a CCFPIFS AD control strategy. Through using the FOPI controller, the CCPIFS AD is extended from the integer-order domain to the fractional-order domain. The damping region of the system is wider than CCPIFS and a degree of control freedom is employed to improve the performance of AD control. By analysing the equivalent virtual impedance of CCFPIFS, the stability constraints of the CCFPIFS AD control strategy are obtained, and the effectiveness of CCFPIFS is verified by Simulink simulation. In terms of the system stability, the damping domain of CCFPIFS is wider on the basis of CCPIFS, the upper limit of the damping domain can be approximated to the Nyquist frequency through parameter selection, and the robustness of the system is enhanced. In terms of the output power quality, with the increase of grid impedance, the output power quality obtained by CCFPIFS is better than that of the CCFS method.

Since the implementation algorithm of fractional-order controllers belongs to another research area, and the truncation error between the analytic solution of the theoretical model and the actual model of the fractional-order controller, as well as the existence of many different discrete and approximate methods, are

worth considering. Our future work is to further improve the performance of the implementation algorithm of the FOPI controller, and it will be applied in practical engineering.

6 References

[1] IEEE Std 519-1992 IEEE recommended practices and requirements for harmonic control in electric power system, IEEE Standards Coordinating Committee, 2004

[2] IEEE Std 1547-2003 IEEE standard for interconnecting distributed resources with electric power system, IEEE Standards Coordinating Committee, 2003

[3] IEEE Std 929-2000 IEEE recommended practice for utility interface of photovoltaic (PV) system, IEEE Standards Coordinating Committee, 2000

[4] Liserre, M., Blaabjerg, F., Hansen, S.: 'Design and control of an LCL-filter-based three-phase active rectifier', *IEEE Trans. Ind. Appl.*, 2005, **41**, pp. 1281–1291

[5] Wu, W., He, Y., Tang, T., *et al.*: 'A new design method for the passive damped LCL - and LLCL-filter based single-phase grid-tied inverter', *IEEE Trans. Ind. Electron.*, 2013, **60**, pp. 4339–4350

[6] Muhlethaler, J., Schweizer, M., Blattmann, R., *et al.*: 'Optimal design of LCL harmonic filters for three-phase PFC rectifiers', *IEEE Trans. Power Electron.*, 2013, **28**, pp. 3114–3125

[7] Wu, W., Liu, Y., He, Y., *et al.*: 'Damping methods for resonances caused by LCL-filter-based current-controlled grid-tied power inverters: an overview', *IEEE Trans. Ind. Electron.*, 2017, **64**, pp. 7402–7413

[8] Pena-Alzola, R., Liserre, M., Blaabjerg, F., *et al.*: 'Analysis of the passive damping losses in LCL-filter-based grid converters', *IEEE Trans. Power Electron.*, 2013, **28**, pp. 2642–2646

[9] Balasubramanian, A.K., John, V.: 'Analysis and design of split-capacitor resistive inductive passive damping for LCL filters in grid-connected inverters', *IET Power Electron.*, 2013, **6**, pp. 1822–1832

[10] Zhang, X., Farina, M., Spinelli, S., *et al.*: 'Multi-rate model predictive control algorithm for systems with fast-slow dynamics', *IET Control Theory Appl.*, 2018, **12**, pp. 2468–2477

[11] He, J., Li, Y.W.: 'Generalized closed-loop control schemes with embedded virtual impedances for voltage source converters with LC or LCL filters', *IEEE Trans. Power Electron.*, 2012, **27**, pp. 1850–1861

[12] Han, Y., Yang, M., Li, H., *et al.*: 'Modeling and stability analysis of LCL-type grid-connected inverters: a comprehensive overview', *IEEE Access*, 2019, **7**, pp. 114975–115001

[13] Zou, C., Liu, B., Duan, S., *et al.*: 'Influence of delay on system stability and delay optimization of grid-connected inverters with LCL filter', *IEEE Trans. Ind. Inf.*, 2014, **10**, pp. 1775–1784

[14] Dannehl, J., Fuchs, F.W., Hansen, S., *et al.*: 'Investigation of active damping approaches for PI-based current control of grid-connected pulse width modulation converters with LCL filters', *IEEE Trans. Ind. Appl.*, 2010, **46**, pp. 1509–1517

[15] Parker, S.G., McGrath, B.P., Holmes, D.G.: 'Regions of active damping control for LCL filters', *IEEE Trans. Ind. Appl.*, 2014, **50**, pp. 424–432

[16] Bao, C., Ruan, X., Wang, X., *et al.*: 'Design of injected grid current regulator and capacitor-current-feedback active-damping for LCL-type grid-connected inverter'. 2012 IEEE Energy Conversion Congress and Exposition (ECCE), Raleigh, North Carolina, USA, 2012, pp. 579–586

[17] Pan, D., Ruan, X., Bao, C., *et al.*: 'Capacitor-current-feedback active damping with reduced computation delay for improving robustness of LCL-type grid-connected inverter', *IEEE Trans. Power Electron.*, 2014, **29**, pp. 3414–3427

[18] Liu, J., Wu, W., Chung, H.S., *et al.*: 'Disturbance observer-based adaptive current control with self-learning ability to improve the grid-injected current for *LCL* -filtered grid-connected inverter', *IEEE Access*, 2019, **7**, pp. 105376–105390

[19] Zhu, K., Sun, P., Wang, L., *et al.*: 'Control delay compensation scheme based on non-instantaneous loading and pulse-width equivalence for active damping of LCL-type inverters', *IET Power Electron.*, 2019, **12**, pp. 2389–2399

[20] Miao, Z., Yao, W., Lu, Z.: 'Single-cycle-lag compensator-based active damping for digitally controlled LCL/LLCL-type grid-connected inverters', *IEEE Trans. Ind. Electron.*, 2020, **67**, pp. 1980–1990

[21] Cai, P., Wu, X., Yang, Y., *et al.*: 'Digital low-pass-filter-based single-loop damping for LCL-filtered grid-tied inverters'. IECON 2018 – 44th Annual Conf. of the IEEE Industrial Electronics Society, Washington, USA, 2018, pp. 6122–6127

[22] Pan, D., Wang, X., Blaabjerg, F., *et al.*: 'Active damping of LCL-filter resonance using a digital resonant-notch (biquad) filter'. EPE'18 ECCE Europe, Portland, Oregon, USA, 2018, pp. 1–9

[23] Liu, T., Liu, J., Liu, Z., *et al.*: 'A study of virtual resistor-based active damping alternatives for LCL resonance in grid-connected voltage source inverters', *IEEE Trans. Power Electron.*, 2020, **35**, pp. 247–262

[24] He, Y., Wang, X., Ruan, X., *et al.*: 'Capacitor-current proportional-integral positive feedback active damping for LCL-type grid-connected inverter to achieve high robustness against grid impedance variation', *IEEE Trans. Power Electron.*, 2019, **34**, pp. 12423–12436

[25] Zheng, W., Luo, Y., Pi, Y., *et al.*: 'Improved frequency-domain design method for the fractional order proportional–integral–derivative controller optimal design: a case study of permanent magnet synchronous motor speed control', *IET Control Theory Appl.*, 2018, **12**, pp. 2478–2487

[26] Pan, D., Ruan, X., Wang, X., *et al.*: 'Analysis and design of current control schemes for LCL-type grid-connected inverter based on a general mathematical model', *IEEE Trans. Power Electron.*, 2017, **32**, pp. 4395–4410

[27] Meng, X., Liu, J., Liu, Z.: 'A generalized droop control for grid-supporting inverter based on comparison between traditional droop control and virtual synchronous generator control', *IEEE Trans. Power Electron.*, 2019, **34**, pp. 5416–5438

[28] Judewicz, M.G., González, S.A., Fischer, J.R.: 'Inverter-side current control of grid-connected voltage source inverters with LCL filter based on generalized predictive control', *IEEE J. Emerg. Sel. Top. Power Electron.*, 2018, **6**, pp. 1732–1743

[29] Pham, T.N., Nahavandi, S., Hien, L.V., *et al.*: 'Static output feedback frequency stabilization of time-delay power systems with coordinated electric vehicles state of charge control', *IEEE Trans. Power Syst.*, 2017, **32**, pp. 3862–3874

7 Appendix

Fig. 16 shows the effect of increasing λ and L_g on the resonance peak of the system. As can be seen in Figs. 16*a–c*, as λ increases, the system bandwidth decreases. When λ is around 1, the amplitude margin and phase margin of the system are both insufficient. When λ decreases from 1, both margins of the system decrease sharply and the system is unstable. In Fig. 16*a*, as the λ increases from 1, both margins of the system are increasing. However, when the value of λ is large, the damping effect on the resonance peak becomes worse, even if the resonance peak exceeds 0 dB, which causes negative phase margins. In Figs. 16*b* and *c*, under the condition of large grid impedance, the system cannot run stably when $\lambda = 1$. With the λ increases from 1, both margins of the system are increasing, and the damping effect on the resonance peak is the first weakened and then increased. From the perspective of stability margin, when λ is small, as the damping effect weakens or even be negative, the system stability margin is insufficient and it is difficult for the system to run stably. When λ becomes larger gradually, the phase characteristics of the system have changed greatly. The initial phase angle and phase transition of the system are different from before, at this time, the system can ensure stable operation. As shown in Fig. 16*d*, with L_g increases, f_r' decreases, and the resonance peak reduces.

Considering Figs. 6 and 16, it can be obtained that due to different λ, the impedance characteristics of the system are different, so the stabilities of the system at different resonance frequencies are also very different. To sum up, when $f_r' > f_s/6$, it only needs to ensure that the amplitude margin and phase angle margin meet the conditions, and the system can run stably. When $f_r' < f_s/6$, with the λ increases from 1, the stability margin of the system becomes larger. As λ continues to increase, the initial phase of the system changes, and the phase-frequency characteristics of the system jump, the system can also run stably. When the amplitude margin of the resonance peak is > 0 dB and the phase angle margin does not jump, the system is unstable.

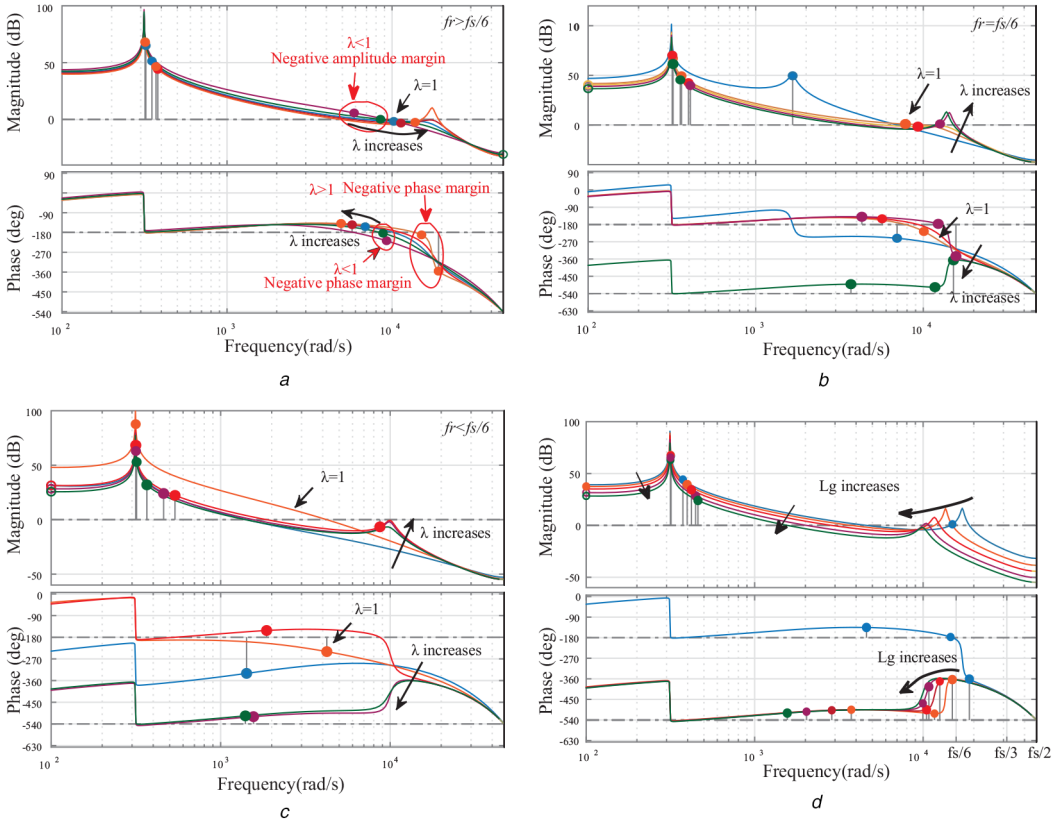

Fig. 16 *Bode diagram of CCFPIFS system open-loop transfer function*

(a), (b), (c) λ increasing, ***(d)*** L_g increasing. (The solid blue line in (a), (b), and (c) corresponds to the system characteristics when $\lambda < 1$, and the solid orange line corresponds to the system characteristics when $\lambda = 1$)